Submitted to *Science Bulletin*

Complete three-dimensional coseismic displacements related to the 2021 Maduo earthquake in Qinghai Province, China from Sentinel-1 and ALOS-2 SAR images

Jihong Liu[1], Jun Hu[1,*], Zhiwei Li[1], Zhangfeng Ma[2], Lixin Wu[1], Weiping Jiang[3], Guangcai Feng[1], Jianjun Zhu[1]

[1] School of Geosciences and Info-Physics, Central South University, Changsha 410083, Hunan, China

[2] School of Earth Sciences and Engineering, Hohai University, Nanjing 211100, Jiangsu, China

[3] GNSS Research Center, Wuhan University, Wuhan 430079, China

*** Corresponding author**

E-mail address: csuhujun@csu.edu.cn (Jun Hu)

Telephone number: +86 13787050426

Submitted to *Science Bulletin*

Abstract

On 21 May 2021, an earthquake struck Maduo county in Qinghai Province, China, which is the largest earthquake to hit China since the 2008 Wenchuan earthquake. In this paper, ascending/descending Sentinel-1 and advanced land observation satellite-2 (ALOS-2) synthetic aperture radar (SAR) images are used to derive the three-dimensional (3-D) coseismic displacements of this earthquake. We employ the differential interferometric SAR (InSAR, DInSAR), pixel offset-tracking (POT), multiple aperture InSAR (MAI), and burst overlap interferometry (BOI) methods to derive the displacements observations along the line-of-sight (LOS) and azimuth directions. To accurately mitigate the effect of ionospheric delay on the ALOS-2 DInSAR observations, a polynomial fitting method is proposed to optimize range-spectrum-split-derived ionospheric phases. Besides, the 3-D displacement field is obtained by an SM-VCE (strain model and variance component estimation) method based on the high-quality SAR displacements observations. Comparison with the global navigation satellite system data indicates that the SM-VCE method can significantly improve the displacements accuracy compared to the classical weighted least square method, and the incorporation of the BOI displacements can substantially benefit the accuracy of north-south displacement. Apart from the displacements, three strain invariants calculated based on the strain model parameters are also investigated. Finally, based on the accurate 3-D coseismic displacements, the source parameters of this event are inverted, revealing four slip asperities with the maximum slip of about 6 m concentrated around the hypocenter. The estimated seismic moment is 1.8×10^{20} Nm, which corresponds to a Mw 7.44 event.

Keywords: The 2021 Maduo earthquake, 3-D displacement, SM-VCE, SAR, Strain field

1 Introduction

At 18:04:13 on 21 May 2021 (UTC), an earthquake of M7.3 struck Maduo county in Qinghai Province, China [1]. This is the largest earthquake to hit China since the 2008 Wenchuan earthquake. The epicenter was located about 38 km southeast of Maduo county at a depth of about 17 km. The earthquake occurred on a known left-lateral strike-slip fault (i.e., Gande south rim fault zone, GDF in Fig. 1) in the northeastern part of the Bayankala block, which is located on the south side of the Kunlun fault. The tectonic background in this region is very complicated, which mainly relates with the northward push of Indian plate, the uplift of the Qinghai-Tibet Plateau block and the eastward extrusion of the Bayankala sub-block. In the past years, there have been several strong earthquakes around the periphery of Bayankala block on the south side of Kunlun fault (e.g., the 2001 M8.1 Kunlun earthquake, the 2008 M8.0 Wenchuan earthquake, the 2010 M7.1 Yushu earthquake, the 2013 M7.0 Lushan earthquake, and the 2017 M7.0 Jiuzhaigou earthquake) [2, 3], and the occurrence of the 2021 M7.3 Maduo earthquake fill the M>7.0 seismic gap around this region (Fig. 1). Field investigations show that this earthquake caused ground surface displacements of up to meters, and induced many cracks, geysers, and seismic bulges.

Ground surface displacement is one of the most intuitive manifestations of earthquakes, and it provides important perspectives for conducting disaster evaluation, constraining the fault slip model, and understanding the triggered mechanism [4]. Synthetic aperture radar (SAR) images that are actively acquired from the satellites can be used to effectively obtain the ground surface displacement field with high accuracy and high spatial resolution [5]. For a pair of SAR images, based on the phase information, the differential interferometric SAR (InSAR, DInSAR) [6] and the multiple aperture InSAR (MAI) [7, 8] methods can obtain the ground surface displacement along the satellite line-of-sight (LOS) and the azimuth (AZI) directions, respectively. In addition, based on the amplitude information of SAR images, the pixel offset-tracking (POT) [9] method can simultaneously obtain the displacement along LOS and AZI directions. Particularly, benefitting from the terrain observation by progressive scans (TOPS) imaging mode of Sentinel-1 SAR data [10], a burst overlap interferometry (BOI) method [11], relying on the phase information, was developed to obtain the AZI displacement for only the overlap area of two successive bursts. In short, with one or more of these methods, it is feasible to obtain a reliable displacement field that can well constrain the fault movement.

In this paper, both Sentinel-1 and advanced land observation satellite-2 (ALOS-2) SAR data from ascending and descending orbits (four pair of SAR images in total) are used to map the complete three-dimensional (3-D) coseismic displacement associated with the 2021 Maduo earthquake. All the above methods (i.e., DInSAR, MAI, BOI, and POT) are used to obtain displacements observations. Since these displacements observations only capture the one-dimensional (1-D) projection of the 3-D displacements along a particular direction (e.g., LOS or AZI), it is difficult to directly relate them to the real surface movements [12-16]. By combining these displacements observations, we calculated the 3-D displacements of the 2021 Maduo earthquake with a newly proposed SM-VCE [17] (a method for measuring 3-D surface displacements with InSAR based on strain model (SM) and variance component estimation (VCE)) method. Previous studies [4, 17, 18] have demonstrated the superiority of the SM-VCE method for estimating more accurate 3-D displacements compared with the classical weighted least squares method. Besides of the ground surface displacements, the surface strain field is another physical quantity that can be used to the relative displacement and subsequent changes in particle configuration in each dimension of the Earth body [19, 20]. There have been a lot of researches on the strain field [e.g., 21, 22-27], most of which are based on traditional geodetic data (e.g., the global navigation satellite system (GNSS) data and the triangulation data). Some open software is also released for the calculation of the strain field based on those sparse observations [e.g., 19, 28, 29]. Here, we calculate three strain invariants based on the strain model parameters and analyze the spatial patter of the strain field in combination with the 3-D displacement field. Finally, a fault slip inversion with

respect to this earthquake is conducted based on the high-accuracy 3-D displacements, and a detailed discussion is provided. Particularly, the displacement result and the fault slip model in this paper can be freely accessed through https://dx.doi.org/10.5281/zenodo.5009820.

2. Materials and methods

2.1. The used SAR data

Since the C-band Sentinel-1 SAR data is acquired regularly and is freely available, it is generally the first choice of SAR data when investigating the displacement with respect to earthquakes, landslides, and so on [e.g., 30, 31]. The L-band ALOS-2 SAR data has a longer wavelength than C-band SAR data and is more capable of suppressing decorrelation noise, so it is also commonly used to measure the surface displacement for earthquakes [e.g., 32, 33]. For the Maduo earthquake, both Sentinel-1 and ALOS-2 SAR data from ascending and descending orbits are available in several days after the earthquake. The basic information of the SAR data used herein is shown in Table 1 and the footprints of these SAR data can be found in Fig. 1.

Table 1. Basic information of the SAR data used herein

Sensor	Orbit direction	Master-slave date	Spatial perpendicular baseline (m)	Wavelength (cm)	Incident angle (deg.)	Azimuth angle (deg.)	Imaging mode
Sentinel-1	As	20210520-20210526	54	5.6	39.5	-13.0	TOPS
Sentinel-1	Des	20210520-20210526	109	5.6	39.6	-167.0	TOPS
ALOS-2	As	20200525-20210524	-190	23.6	36.2	-12.7	Strip-map
ALOS-2	Des	20201204-20210604	197	23.6	39.0	-170.0	ScanSAR

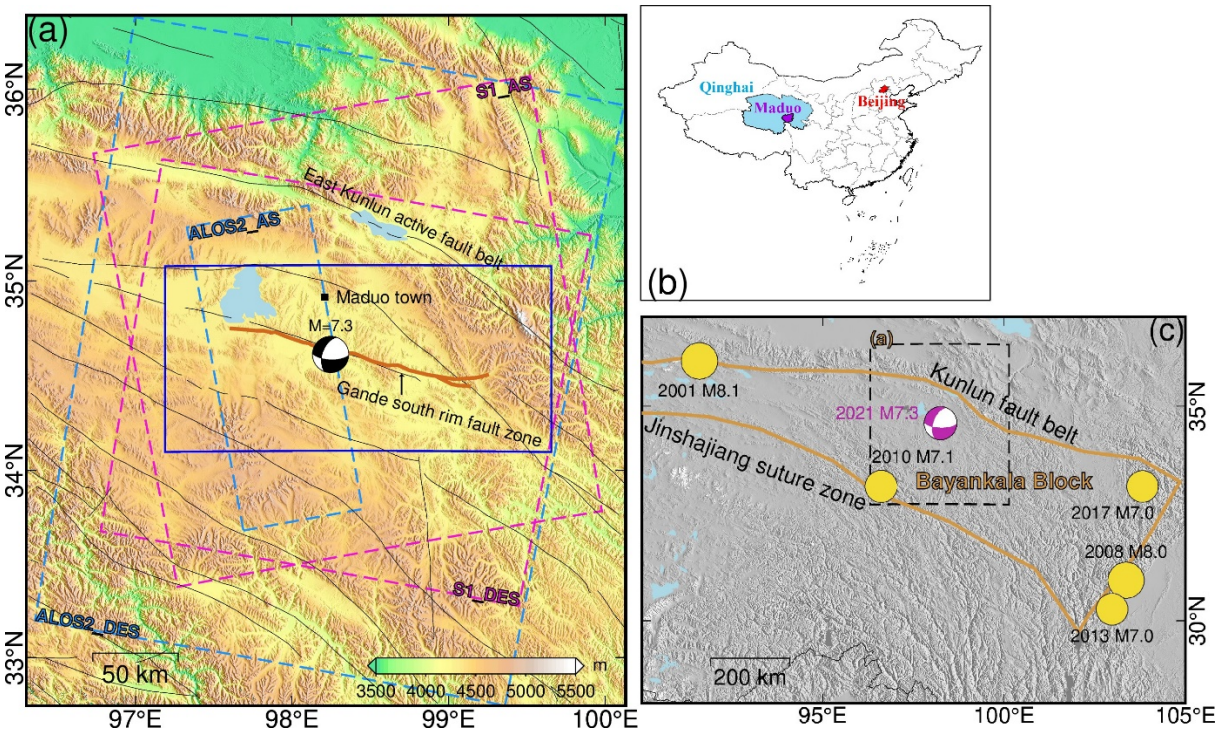

Fig. 1. (a) Colour shaded relief map. The dashed rectangles outline the footprint of SAR data, and the blue rectangle outlines the focused study area (e.g., the range in Fig. 2 and Fig. 4) in this paper. The black lines show the location of known faults, where the east Kunlun active fault belt and the Gande south rim fault zone are labeled. The brown lines are the ruptured fault traces of the 2021 Maduo earthquake, which are manually sketched based on the Sentinel-1 POT observations. The beach ball represents the focal mechanism and epicenter location from the USGS. The location of the Maduo town is represented by the black square. (b) shows the relative position of the Maduo county in Qinghai Province in China. (c) The distribution of M>7.0 earthquakes around the 2021 Maduo earthquake in the east part of the Bayankala block. The dished rectangle outlines the range of (a).

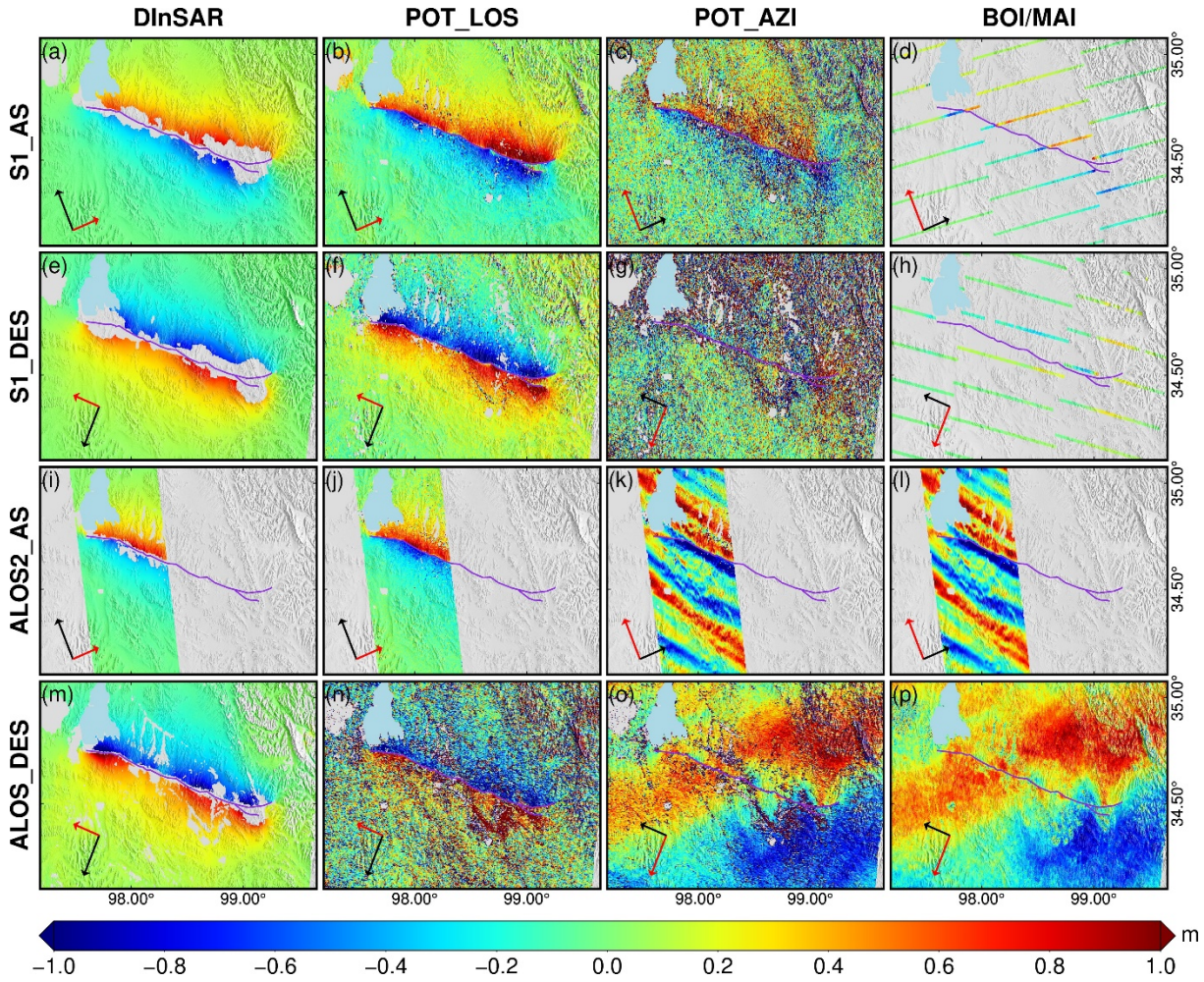

Fig. 2. Displacements observations along the LOS and AZI directions from ascending/descending, Sentinel-1/ALOS-2 SAR data based on the DInSAR, POT, MAI and BOI methods. Longer and shorter arrows represent the AZI and LOS directions, respectively, and the red arrow corresponds to the observing direction of each observation. The purple lines show the location of ruptured fault traces. The displacements within the range of the whole SAR image are shown in Fig. S1.

Here, the DInSAR, MAI, POT, and BOI methods are employed to process the ascending/descending Sentinel-1/ALOS-2 SAR images, and the detailed processing procedure can be found in Text S1. Fig. 2 presents the obtained SAR displacements observations. For the sake of simplicity, the combination of several abbreviations linked by underlines is used to represent the corresponding SAR displacement observation. For example, ALOS2_AS_DInSAR represents the DInSAR observation of ascending (AS) ALOS-2 data. As shown in Fig. 2, the displacements observations with the similar geometry are consistent with each other (e.g., the S1_DES_DInSAR (Fig. 2(e)), ALOS2_DES_DInSAR (Fig. 2(m)), and S1_DES_POT_LOS (Fig. 2(f)),). Due to the longer wavelength of the ALOS-2 data compared to the Sentinel-1 data, the measurable displacement gradient of DInSAR method of the ALOS-2 data is higher than Sentinel-1 data, therefore the ALOS2_DInSAR observations (Fig. 2(i) and Fig. 2(m)) can obtain more complete displacement field in the near-fault regions compared to the S1_DInSAR observations (Fig. 2(a) and Fig. 2(e)). However, the ALOS-2 data suffer serious ionospheric disturbs (Fig. 2(k), Fig. 2(l), Fig. 2(o) and Fig. 2(p)), and its effect on the DInSAR observations cannot be ignored. Although a range spectrum split (RSS) method can be used to estimate the ionospheric phase, it is very sensitive to the decorrelation noise. In this paper, a polynomial fitting (PolyFit) method is proposed to optimize the RSS-derived ionospheric phase especially in the low-coherence near-fault regions. Detailed of the proposed method can be

found in section 2.2. Through qualitative comparison, the accuracy of the POT observations is lower than the DInSAR and BOI observations, and is proportional to the pixel resolution. One prominent advantage of the POT method lies that it can obtain complete displacement field even in the DInSAR decorrelated regions [e.g., 34, 35].

2.2 The polynomial fitting method for correcting the ionospheric phase delay

The proposed PolyFit method obtains the ionospheric phase based on the low-accuracy RSS-derived ionospheric phases (Fig. 3(b)), in which those regions with strong ionospheric fluctuations are first masked (Fig. 3(c)). As can be seen from Fig. S2, the ionospheric phases in the SAR LOS displacements observations are generally low-pass signals in small regions, therefore can be fitted by polynomials. In this case, the ionospheric phases can be optimized and recovered in the whole region (Fig. 3(d)) based on the RSS ionospheric phases in the unmasked regions.

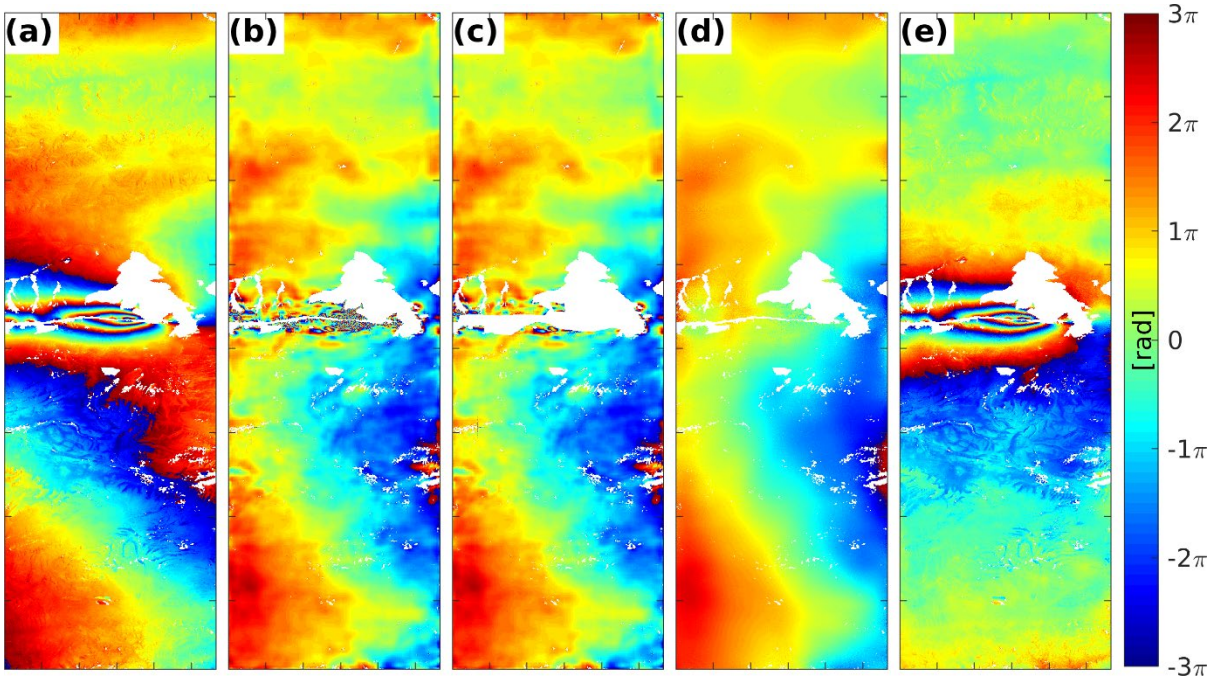

Fig. 3. An example of the proposed filtering and interpolating strategy for the ionospheric delay correction with respect to the third beam of the descending ALOS-2 data. (a) The original interferogram. (b) The original RSS-derived ionospheric phase. (c) The original RSS-derived ionospheric phase with the strong fluctuation regions being masked. (d) The ionospheric phase derived by the proposed filtering and interpolating strategy. (e) The interferogram after the ionospheric phase correction. These unwrapped phases are rewrapped here for better display.

We assume there are K valid pixels (x_k, y_k), $k = 1,2,\dots,K$ around a target pixel (x_0, y_0), and the original RSS-derived ionospheric phases at those K pixels are $\boldsymbol{\varphi}_{\mathrm{rss}} = \left[\varphi_{\mathrm{rss},1}, \varphi_{\mathrm{rss},2}, \dots, \varphi_{\mathrm{rss},K}\right]^T$. Let

$$\boldsymbol{B}_{\mathrm{rss}} = \begin{bmatrix} 1 & x_1 & y_1 \\ 1 & x_2 & y_2 \\ \vdots & \vdots & \vdots \\ 1 & x_K & y_K \end{bmatrix} \tag{1}$$

the fitting polynomial parameters $\boldsymbol{x}_{\mathrm{poly}}$ can be estimated based on the least square method

$$\boldsymbol{x}_{\mathrm{poly}} = (\boldsymbol{B}_{\mathrm{rss}}^T \boldsymbol{B}_{\mathrm{rss}})^{-1} \boldsymbol{B}_{\mathrm{rss}}^T \boldsymbol{\varphi}_{\mathrm{rss}} \tag{2}$$

In this case, the optimized ionospheric phase $\hat{\varphi}_{\mathrm{rss},0}$ at the target pixel (x_0, y_0) can be obtained by

$$\hat{\varphi}_{\mathrm{rss},0} = [1 \quad x_0 \quad y_0] \cdot \boldsymbol{x}_{\mathrm{poly}} \tag{3}$$

Note that the PolyFit method is conducted on a pixel-by-pixel basis. In addition, the second-order polynomial, rather than the first-order polynomial used in Eq. (1), can be used if spatial variation of the ionospheric delay is very complicated. The ionospheric phases in the mask regions can be recovered by the surrounding valid signals. Furthermore, it is crucial to determine the maximum distance between the surrounding K pixels and the target pixel. Since the spatial variation of ionospheric delay can't be previously determined, it is difficult to set a fixed threshold for maximum distance. Alternatively, it is recommended to determine the maximum distance by considering the real spatial pattern of the ionospheric delay. For example, given that the size of the whole region in Fig. 3 is 3910×1132, the maximum distance is empirically set as 150 pixels. Fig. S2 shows the ALOS2_DES_DInSAR observation before and after the ionospheric delay correction, where the ionospheric phases have been significantly mitigated.

2.3 The SM-VCE method

In this paper, an SM-VCE method [17] is employed to calculate the 3-D displacements of the 2021 Maduo earthquake based on the above SAR displacements observations. Traditionally, the 3-D displacements at a target point are calculated from those displacements observations at this target point based on a weighted least square (WLS) method [e.g., 12, 13, 15, 35], where the weights of these observations are determined based on the far-field observations that are assumed to be free of displacements or on the standard deviation of observations in a 5×5 pixels window around the target point [e.g., 15, 36]. However, for a geophysical process (e.g., the earthquake), the ground surface displacements at adjacent points are generally correlated (apart from the fault ruptured regions). The ignorance of this correlation is unreal and limits the 3-D displacements to a higher accuracy. Also, the empirical weighing strategies cannot precisely reflect the accuracy of observations and result in the reduced accuracy of the 3-D displacements. In the SM-VCE method [17], the strain model (SM) [37] is employed to represent the correlation between adjacent points' displacements, and the weights of different observations are determined by the well-known variance component estimation (VCE) algorithm [38]. In this case, the SM-VCE method is more accurate for obtaining 3-D displacements compared to the traditional WLS method [4, 17, 18]. For completeness, Text S2 introduces the basic principles of the SM-VCE method, and the obtained 3-D displacements of the 2021 Maduo earthquake can be found in section 3.

In the SM-VCE method, the number of adjacent points in the limited range is vital for the accuracy and efficiency of the method. In this case study, the window size is empirically determined as 61×61 pixels since in this spatial scale the displacement-to-noise ratio of the POT-derived observations is sufficient for obtaining reliable 3-D displacements. Since obvious displacement jumps occurred across the fault region (see Fig. 2), it is impracticable to use all the available observations in the predefined window for the calculation of the 3-D displacements near the fault region. Based on the POT-derived observations (e.g., Fig. 2(b) and Fig. 2(f)), the fault traces can be manually mapped and then be used to exclude the observations on the opposite side of the fault when calculating the 3-D displacements near the fault regions.

3. Results

The 3-D displacements of the 2021 Maduo earthquake are obtained from the eleven ascending/descending Sentinel-1/ALOS-2 SAR displacements observations based on the SM-VCE method. As shown in Fig. 4, the east-west (E-W) displacement component dominates the ground surface movements of the 2021 Maduo earthquake, with the maximum eastern and western displacements of 1.7 m and 2.4 m, respectively. Besides, it seems that the

epicenter region suffers the slighter E-W displacements along the fault trace, and the magnitude of E-W displacement becomes larger from the epicenter region to the eastern and to the western regions. Based on the 3-D displacement field, it is easy to infer that the overall displacement pattern of this earthquake is consistent with the left-lateral strike-slip fault, and the largest horizontal displacements occurred around eastern region of the main fault with the magnitude of 2.4 m. One interesting displacement pattern is around the northern side of the eastern end of the faults, where the horizontal displacements, especially the north-south (N-S) displacements, seem to encounter a barrier that changes the displacement direction from southwest to northwest. Compared with the E-W and N-S displacement components, the vertical displacement component is more concentrated in the near-fault regions and the magnitude is smaller.

The near-field global navigation satellite system (GNSS) horizontal coseismic displacements (see the circles in Fig. 4) are used to assess the accuracy of the SAR-derived 3-D displacements. The root mean square errors (RMSEs) between the GNSS and the SAR-derived displacements are 5.2 cm and 12.2 cm in the E-W and N-S components, respectively. The RMSE value in the north component is relatively large. This might be biased by the GNSS station near the fault trace closest to the epicenter, where the difference in the N-S displacement between GNSS and SAR is up to 35 cm. This bias may be partly due to the very local ground fracture at this GNSS station caused by the strong seismic vibration. We re-evaluate the accuracy by excluding this site, resulting in the RMSE value of 6.4 cm for the north component. For comparison, the classical WLS method is also used to estimate the 3-D displacements of the 2021 Maduo earthquake. As shown in Fig. S3, the WLS-derived 3-D displacements are much noisier compared to the SM-VCE result (Fig. 4). The RMSEs between the GNSS and WLS-derived displacements are 9.3 cm and 37.0 cm in the E-W and N-S components, respectively, which indicates that improvements of 44% and 83% can be achieved in this case study by the SM-VCE method for the E-W and N-S components, respectively.

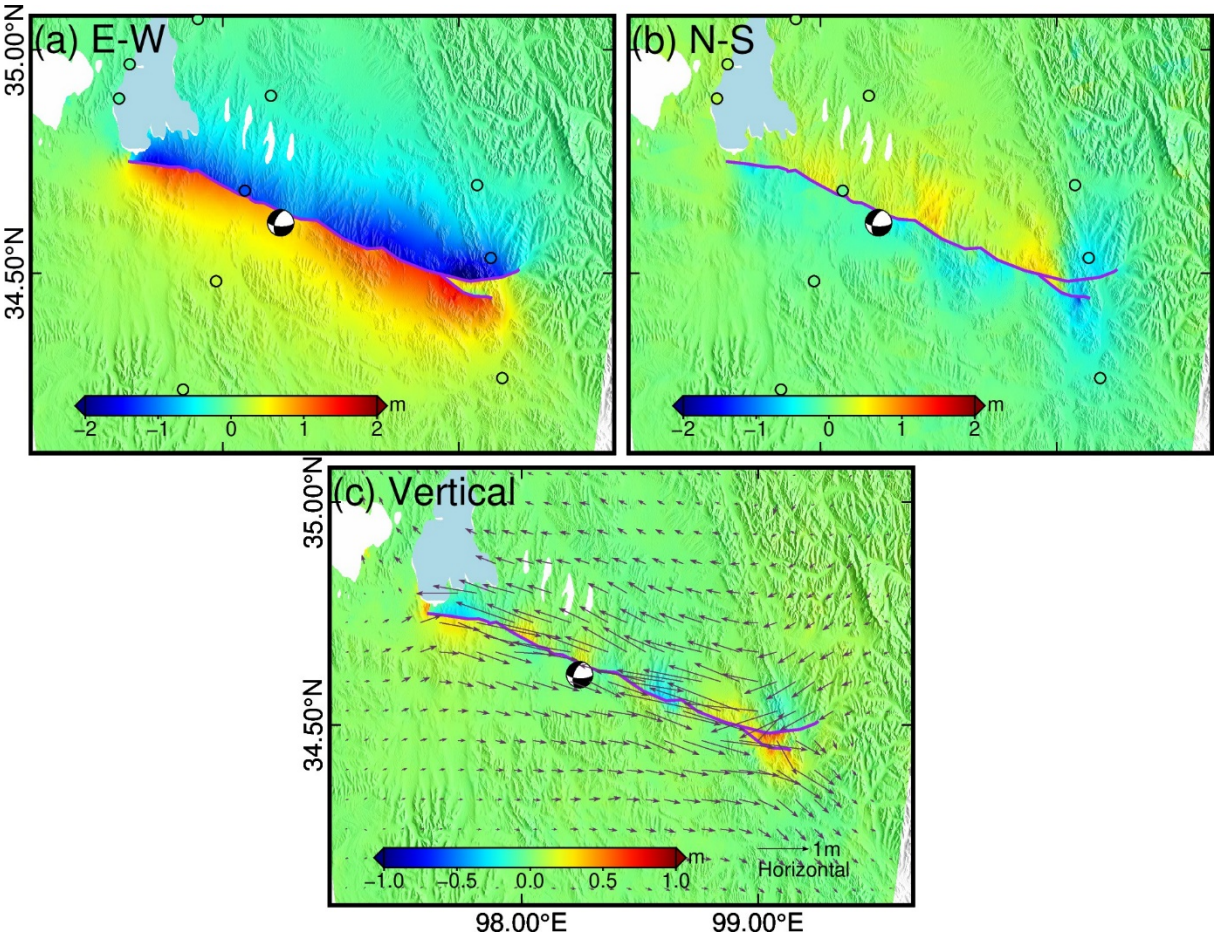

Fig. 4. Three-dimensional coseismic displacements of the 2021 Maduo earthquake derived by SM-VCE method. Circles in (a) and (b) show the locations of the GNSS stations, and their color indicates the GNSS-observed displacement. The arrows in (c) are the down-sampled horizontal displacements. The 3-D displacements within a greater range are shown in Fig. S4.

4. Discussion

4.1 The importance of BOI observations for the N-S displacement component

Since BOI method can only obtain AZI displacements in the burst overlap area, this method is not a commonly used method for displacement monitoring like the DInSAR, MAI, and POT methods. However, some cases have demonstrated that this method can provide important AZI displacement information [e.g., 11, 39-41], particularly for the earthquakes. Among the SAR displacements observations for the 2021 Maduo earthquake in this paper, except the BOI observations, the N-S displacement component can only be well constrained by the S1_POT_AZI observations. However, the accuracy of the S1_POT_AZI observations is too low to obtain high precision N-S displacement. Therefore, it is expected that the BOI observations with higher accuracy compared to the S1_POT_AZI is of great insignificant in the calculation of N-S displacement.

To illuminate the importance of BOI observations for the N-S displacement component, the 3-D displacements are calculated by the SM-VCE method without the BOI observations. As shown in Fig. S5, it is found that the spatial pattern is very similar between the 3-D displacements in Fig. S5 (without the BOI observations) and in Fig. 4 (with the BOI observations). However, the N-S displacement component is noisier when the BOI observations are not used. Comparing with the GNSS data, the RMSE values are 5.4 cm and 13.7 cm for the E-W and N-S displacement components, respectively, illuminating that significant improvement of about 53% can be achieved for the N-S component in this study when the BOI observations are combined.

At present, most applications of the BOI method are for large magnitude of displacements (e.g., earthquakes) with only one pair of SAR images. By combining the SAR time-series data, some researchers attempt to obtain the millimeter-level AZI displacements with respect to the plate inter-seismic movement [42, 43]. This achievement is substantially exciting since such a small magnitude of displacement can only be captured by the multi-temporal InSAR (MT-InSAR) method which is only sensitive to the E-W and vertical components. The AZI displacements observations obtained by the BOI method can well complement the DInSAR-derived observations, and then can be used to realize time series of 3-D displacements monitoring. Benefiting from the open data policy and the regular acquisition of Sentinel-1 data, the BOI method can gradually become a routine tool for displacement monitoring, therefore providing important displacements observations for various geohazards.

4.2 Three strain invariants from the strain model

Besides of the ground surface displacements, the surface strain fields can also be used to interpretate and describe the real geophysical behavior associated with seismic activities [24]. Strain describes the non-rigid body deformation, which is a geometric concept to quantify the relative displacement and subsequent changes in particle configuration in each dimension of the body [19]. For the deformation analysis of non-rigid body, three 2-D (i.e., the horizontal plane) strain invariants (i.e., dilatation, differential rotation, and maximum shear) with physical meaning are generally preferred [21, 25, 26, 29], which are independent of any shift and rotation of the coordinate systems. The dilatation invariant corresponds to the volume compression and extension of the Earth body. For example, if the horizontal displacements of surround points are towards or away from a point, the dilatation represents the volume compression and extension, respectively, and the dilatation value at this point is negative or positive, respectively. The differential rotation represents the rotating trend of the horizontal displacements. If the

horizontal displacements are towards the same direction within a region, the rotation value would be zero. However, when the horizontal displacements gradually deviate from their current displacement direction, the rotation value would donate the direction and magnitude of the rotation. As for the maximum shear, it is generated in the region where relative displacements occur. For example, if the direction of the horizontal displacements of adjacent two points is similar, but the magnitude is different, there would be the maximum shear strain along the displacement direction.

Detailed calculation of these three strain invariants can be found in Text S3 and Fig. 5 presents the calculated strain invariants of the 2021 Maduo earthquake. For the dilatation map (Fig. 5(a)), positive and negative values represent the regions experiencing extensional and compressional deformations, respectively. The crosses represent the maximum and minimum normal strains, where the arrow orientation and the arrow length indicate the direction and magnitude of the strains, respectively. The extensional and compressional strains are shown as the inward and outward arrows, respectively. The eastern and western parts of the faults experience the most serious extensional and compressional deformations. This phenomenon is expected since the horizontal displacements change dramatically in these regions (see Fig. 4). Besides, the region corresponding to extensional or compressional deformation is generally dominated by the extensional strain (the outward arrow) or the compressional strain (the inward arrow). In the differential rotation map (Fig. 5(b)), the negative value means the clockwise rotation and the rotational wedges aim to better illuminate the magnitude and direction of the rotation. Both sides of the main faults experience the similar clockwise rotation, which is consistent with the horizontal displacement pattern where the horizontal displacements gradually deviate to the right of their current displacement direction. The magnitude of rotation is large near the fault, and decreases with the distance from the fault. Similarly, due to the dramatically changed horizontal displacements in the eastern and western parts of the faults, the rotation magnitude is very large in these regions. As for the maximum shear map (Fig. 5(c)), the double-sided arrow represents the direction of the maximum shear, which is generally parallel to the orientation of the main fault. Also, the shear signals concentrate near the fault trace, and decrease with the distance from the fault. Combining Fig. 5(b) and Fig. 5(c) reveals an interesting phenomenon that the strain magnitude round the epicenter is smaller than that of other regions near the fault, which may be attributed to the smaller magnitude of slip around the hypocenter (Fig. 6).

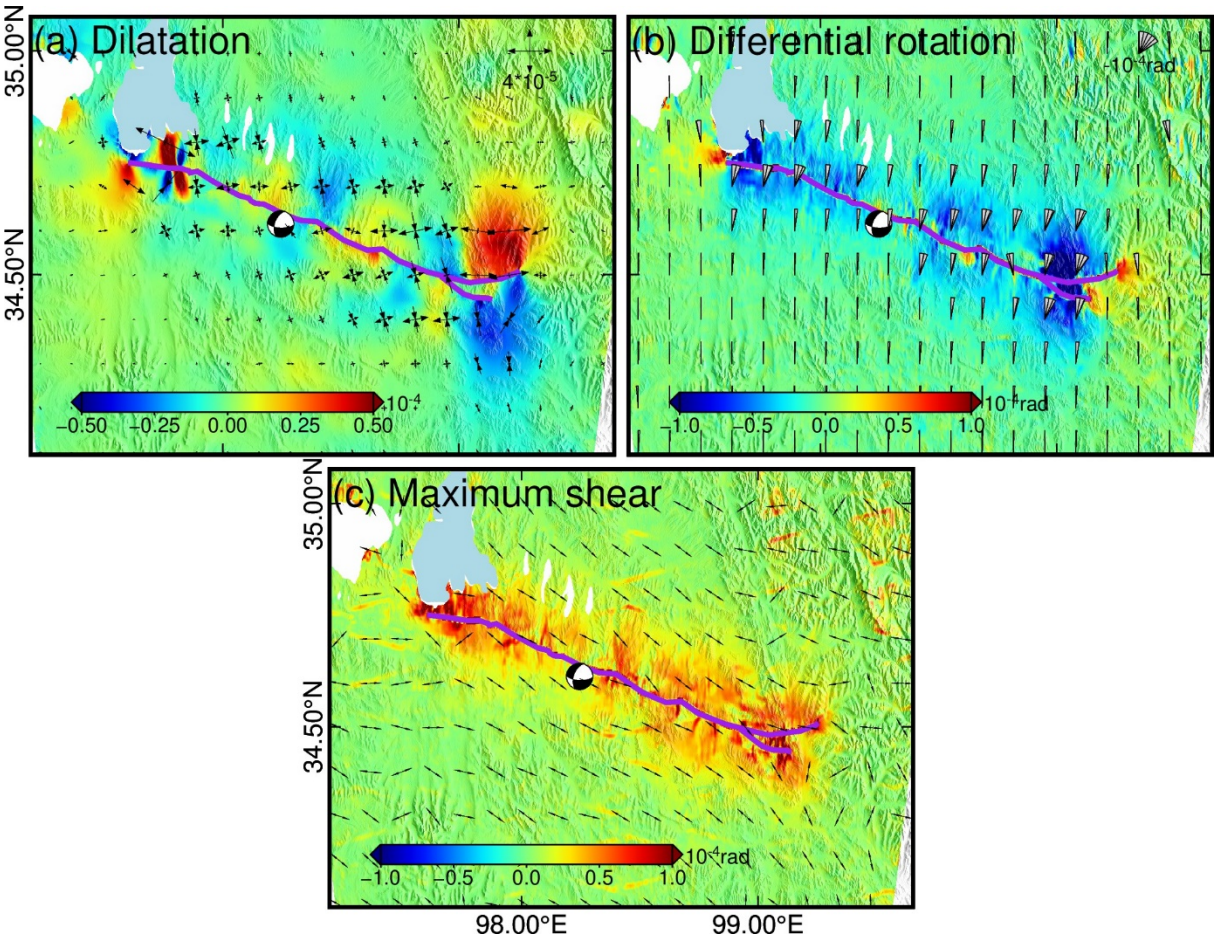

Fig. 5. Three strain invariants for the 2021 Maduo earthquake. In (a), the crosses represent the maximum and minimum normal strains, where the arrow orientation and the arrow length are the direction and magnitude of the strains, respectively. The extensional and compressional strains are shown as the inward and outward arrows, respectively. In (b), the rotational wedges are presented to better illuminate the magnitude and direction of the rotation. In (c), the direction of the double-sided arrow represents the direction of the maximum shear. The strain fields within a greater range are shown in Fig. S6.

4.3 Slip model based on the derived 3-D displacements

We used the 3-D coseismic displacements to inverse fault parameters and slip distribution at depth. We assume these displacement maps are independent of each other in the modeling [44]. In the inversion, we used triangle dislocations [45] in a homogeneous and elastic Poisson half-space (Poisson's ratio $\nu = 0.25$). Focal mechanism solutions for the 2021 Maduo earthquake provided by USGS indicate that the slip probably occurred on a nearly vertical fault striking from west-north (WN) to east-south (ES). From the derived E-W displacement map (Fig. 4(a)), a roughly WN-ES trending fault trace separates displacements at opposite directions nearly throughout the entire fault system. Moreover, the N-S displacement map also presents in the opposite direction (Fig. 4(b)). Given the clearly mapped fault track, we back up the opinion that the slip occurs on a WN-ES trending left-lateral fault. Visual inspection on the vertical displacement map (Fig. 4(c)) indicates that only a little rift and subsidence can be observed around the fault trace. We suppose that the strike slip dominates the slip distribution. Through further investigating on the displacement maps, we infer the occurrence of two fault segment traces. We marked the fault traces out for determining the fault striking direction. After determining two fault traces, we determined two different rake angles in geodetic inversion. A rake angle ranging from -30° and 30° was set for the relatively long

fault, while a rake angle ranging from of -60° and 60° was set for the short fault as the near-field displacement map along it did not show the same obvious left-lateral strike-slip characteristics as the long one. Preliminary USGS earthquake report suggested that the earthquake obviously ruptured the surface. Therefore, the top depths of two faults were set to 0 km. Each fault width along dip was set as 18 km. In addition, we discretized two fault segments into irregular triangle patches with different size in order to represent shallow slip as much as possible. We used the trade-off curve method to determine the dip angles of these two faults, and the dip angles of both these two faults are 90° (Fig. S7). An adaptive downsample method based on the fault model was applied to downsample the 3-D displacements and calculate the covariance [46]. The final downsampled datasets include 8670 triangles (Fig. S8). To approach the realistic of slip estimation as much as possible, we applied an automatic Laplacian smooth factor in the inversion process. A constrained least squares method was employed to invert the final slip distribution [47, 48]. In addition to the geodetic inversion, we also conduct a bootstrapping test method to calculate the slip model uncertainty of the inverted slip distribution due to possible random noise in our derived 3-D displacement maps [49]. We give a detailed description on geodetic inversion process and further on this bootstrapping test in Text S4-S5.

Our derived slip distribution is shown in Fig. 6. The related modeled deformation and the corresponding residuals are shown in Fig. S9. The calculated slip model uncertainty (Fig. S10) are all less than 3 cm. It directly validates our slip model can well resist the perturbation of errors that may exist in our derived 3-D displacements. USGS inverted the co-seismic slip based on the P/SH waveforms and long period surface waves data using a finite fault inversion method [50]. Preliminary coseismic slip model based on a nodal plane (strike = 106.0°; dip = 76.0°) reports a 1.3×10^{20} Nm seismic moment release, which is equal to a Mw 7.4 event. The derived two-faults slip model in this study (average strike = 102.1°; dip = 90.0°) is slightly different from it. We report a 1.8×10^{20} Nm seismic moment release, which corresponds to a Mw 7.44 event. Slightly large seismic moment can be explained by that the used Sentinel-1 and ALOS-2, which are acquired at least 3 days after the earthquake event, would introduce the components of aftershocks and early post-seismic deformation into the derived 3-D displacements. Consistent with the preliminary slip model provided by USGS, the slip model derived in this study also indicates four slip asperities around the hypocenter. The largest asperity of ~40 km^2 with a maximum slip of 6 m is close to the hypocenter. These asperities all concentrated in the shallow layers (<5km). However, the patches deeper than 5km present little slip. It may indicate potential earthquake risks can be triggered by these places. Further studies on the seismic moment released by post-seismic deformation and afterschocks are needed. It should be noted that the discrepancy between the slip model based on 3-D displacements and the USGS slip model based on seismic waveforms data probably reflect the heterogeneity and complexity of this fault system.

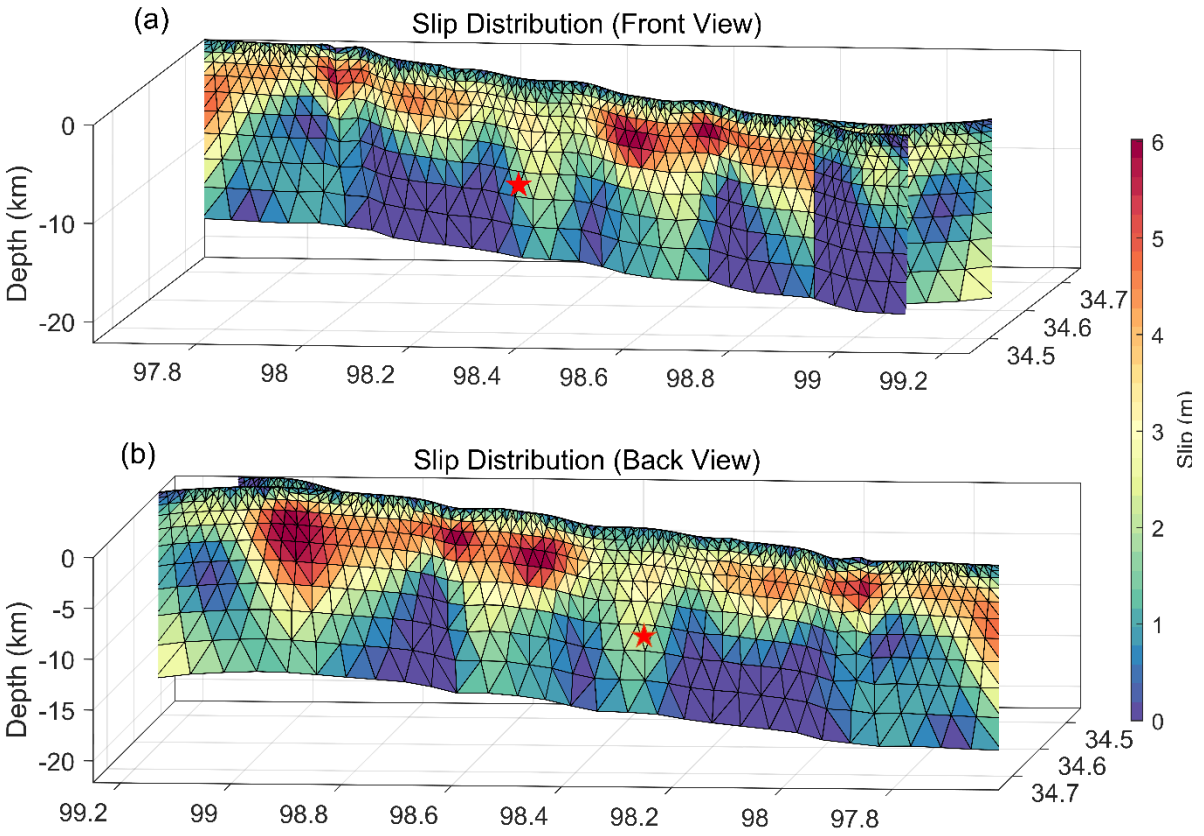

Fig. 6. Slip distribution derived from the constraints of our derived 3-D displacements. (a) is the front view of the slip distribution of two faults. (b) is the back view for a better view on the long fault. Red stars represent the location of hypocenter.

5. Conclusions

The 2021 Maduo earthquake, Qinghai Province, China is the largest earthquake to hit China since the 2008 Wenchuan earthquake. In this paper, we derive the complete 3-D coseismic displacements associated with this earthquake using both C-band Sentinel-1 and L-band ALOS-2 SAR data from ascending/descending tracks. Up to eleven high quality SAR displacements observations in the geometries of ascending/descending LOS/AZI directions are obtained based on the DInSAR, POT, BOI, and MAI methods. Since the RSS-derived ionospheric phases are very sensitive to the decorrelation noise, a filtering and interpolating strategy is proposed to correct the ionospheric phase delay in the L-band ALOS-2 DInSAR interferograms. The accurate 3-D displacement field of the 2021 Maduo earthquake is obtained by the SM-VCE method to intuitively reveal the real ground surface movement. It is found that this earthquake is dominated by the left-lateral fault slip with the largest horizontal displacement of up to 2.4 m. Comparison with the GNSS data indicates that the SM-VCE method can significantly improve the horizontal displacements compared to the classical WLS method, and the incorporation of the BOI displacements can substantially benefit the accuracy of N-S displacement component. Based on the high-accuracy 3-D displacements, the fault slip distribution is inverted. In addition to the surface displacement, the strain field is another physical quantity that can be used to quantify the relative displacement within the Earth body. Based on the strain model parameters estimated by the SM-VCE method, three strain invariants (i.e., dilatation, differential rotation, and maximum shear) are calculated and analyzed. Results show that the eastern and western parts of the faults suffer serious strains, but the epicenter region is less affected by the rotation and shear strains. The displacement result and the fault slip model in this paper in this paper can be freely accessed, which will be useful

for a broad community studying this earthquake.

Conflict of interest

The authors declare that they have no conflict of interest.

Acknowledgments

The ALOS-2 data were provided by the Japan Aerospace Exploration Agency (JAXA) (https://auig2.jaxa.jp/ips/home, PI No. PER2A2N038), and the Sentinel-1 data were provided by ESA/Copernicus (https://scihub.copernicus.eu/). We would like to thank Prof. Guoyan Jiang for his help in geophysical inversion. This work was supported by the National Key Basic Research and Development Program of China (No. 2018YFC1503603), the National Natural Science Foundation of China (No. 42030112), the Nature Science Foundation of Hunan Province (No. 2020JJ2043), the Project of Innovation-driven Plan of Central South University (No. 2019CX007), by the Fundamental Research Funds for the Central Universities of Central South University (Nos. 2018zzts684 and 2019zzts011), and by the Hunan Provincial Innovation Foundation For Postgraduate (No. CX20190067). The displacement result and the fault slip model in this paper can be freely accessed through https://dx.doi.org/10.5281/zenodo.5009820.

Author contributions

J. Liu, J. Hu, Z. Li, and Z. Ma conceived the experiment; J. Liu and Z. Ma performed the experiments and data analysis with the assistance of J. Hu, Z. Li, L. Wu, and J. Zhu; J. Liu wrote the first draft of the manuscript. J. Hu and G. Feng provided the data and supervised the experiments; W. Jiang coordinated the project and supervised the data analysis of the work; All the authors contributed extensively to the work presented in this paper.

Electronic supplementary materials

Supplementary figures to this article can be found online at https://doi.org/xxxxxx.

References

[1] Li Y, Huang L, Ding R, et al. Coulomb stress changes associated with the m7. 3 maduo earthquake and implications for seismic hazards. Nat Hazard Res 2021.

[2] Zhu Y, Diao F, Fu Y, et al. Slip rate of the seismogenic fault of the 2021 maduo earthquake inferred from gps observations. SCIENCE CHINA Earth Sciences 2021;64.

[3] Wang W, Fang L, Wu J, et al. Aftershock sequence relocation of the 2021 ms7.4 maduo earthquake, qinghai, china. SCIENCE CHINA Earth Sciences 2021;64.

[4] Hu J, Liu J, Li Z, et al. Estimating three-dimensional coseismic deformations with the sm-vce method based on heterogeneous sar observations: Selection of homogeneous points and analysis of observation combinations. Remote Sens Environ 2021;255:112298.

[5] Tian Y, Liu-Zeng J, Luo Y, et al. Transient deformation during the milashan tunnel construction in northern sangri-cuona rift, southern tibet, china observed by sentinel-1 satellites. Science Bulletin 2018;63:1439-1447.

[6] Gabriel AK, Goldstein RM, Zebker HA. Mapping small elevation changes over large areas: Differential radar interferometry. J Geophys Res Solid Earth 1989;94:9183-9191.

[7] Bechor NBD, Zebker HA. Measuring two-dimensional movements using a single insar pair. Geophys Res Lett 2006;33:275-303.

[8] Jung HS, Won JS, Kim SW. An improvement of the performance of multiple-aperture sar interferometry (mai). IEEE Trans Geosci Remote Sens 2009;47:2859-2869.

[9] Michel R, Avouac JP, Taboury J. Measuring ground displacements from sar amplitude images: Application to the landers earthquake. Geophys Res Lett 1999;26:875-878.

[10] Torres R, Snoeij P, Geudtner D, et al. Gmes sentinel-1 mission. Remote Sens Environ 2012;120:9-24.

[11] Grandin R, Klein E, Métois M, et al. 3d displacement field of the 2015 m w 8.3 illapel earthquake (chile) from across- and along-track sentinel-1 tops interferometry. Geophys Res Lett 2016;43:2552-2561.

[12] Wright TJ, Parsons BE, Lu Z. Toward mapping surface deformation in three dimensions using insar. Geophys Res Lett 2004;31:169-178.

[13] Fialko Y, Sandwell D, Simons M, et al. Three-dimensional deformation caused by the bam, iran, earthquake and the origin of shallow slip deficit. Nature 2005;435:295-299.

[14] Funning GJ, Parsons B, Wright TJ, et al. Surface displacements and source parameters of the 2003 bam (iran) earthquake from envisat advanced synthetic aperture radar imagery. J Geophys Res Solid Earth 2005;110.

[15] Jung HS, Lu Z, Won JS, et al. Mapping three-dimensional surface deformation by combining multiple-aperture interferometry and conventional interferometry: Application to the june 2007 eruption of kilauea volcano, hawaii. IEEE Geosci Remote Sens Lett 2011;8:34-38.

[16] He P, Wen Y, Xu C, et al. Complete three-dimensional near-field surface displacements from imaging geodesy techniques applied to the 2016 kumamoto earthquake. Remote Sens Environ 2019;232:111321.

[17] Liu J, Hu J, Li Z, et al. A method for measuring 3-d surface deformations with insar based on strain model and variance component estimation. IEEE Trans Geosci Remote Sens 2018;56:239-250.

[18] Liu J, Hu J, Xu W, et al. Complete three-dimensional co-seismic deformation fields of the 2016 central tottori earthquake by integrating left- and right-looking insar with the improved sm-vce method. J Geophys Res Solid Earth 2019;124:12099–12115.

[19] Cardozo N, Allmendinger RW. Sspx: A program to compute strain from displacement/velocity data. Comput Geosci 2009;35:1343-1357.

[20] Okada Y. Surface deformation to shear and tensile faults in a halfspace. Bull Seismol Soc Am 1985;75:1018-1040.

[21] Shen Z-K, Jackson DD, Ge BX. Crustal deformation across and beyond the los angeles basin from geodetic measurements. J Geophys Res Solid Earth 1996;101:27957-27980.

[22] Clarke PJ, Davies RR, England PC, et al. Crustal strain in central greece from repeated gps measurements in the interval 1989-1997. Geophys J Int 1998;135:195-214.

[23] Pietrantonio G, Riguzzi F. Three-dimensional strain tensor estimation by gps observations: Methodological aspects and geophysical applications. J Geodyn 2004;38:1-18.

[24] Savage JC, Lisowski M. Strain accumulation north of los angeles, california, as a function of time, 1977–1992. Geophys Res Lett 1994;21:1173-1176.

[25] Lin KC, Hu JC, Ching KE, et al. Gps crustal deformation, strain rate and seismic activity after the 1999 chi-

chi earthquake in taiwan. J Geophys Res Solid Earth 2010;115:1-22.

[26] Mehrabi H. Three-dimensional strain descriptors at the earth's surface through 3d retrieved co-event displacement fields of differential interferometric synthetic aperture radar. J Geod 2021;95:1-16.

[27] Hu J, Wang QJ, Li ZW, et al. Retrieving three-dimensional coseismic displacements of the 2008 gaize, tibet earthquake from multi-path interferometric phase analysis. Nat Hazards 2014;73:1311-1322.

[28] Teza G, Pesci A, Galgaro A. Grid_strain and grid_strain3: Software packages for strain field computation in 2d and 3d environments. Comput Geosci 2008;34:1142-1153.

[29] Goudarzi MA, Cocard M, Santerre R. Geostrain: An open source software for calculating crustal strain rates. Comput Geosci 2015;82:1-12.

[30] Funning GJ, Garcia A. A systematic study of earthquake detectability using sentinel-1 interferometricwide-swath data. Geophys J Int 2019;216:332-349.

[31] Intrieri E, Raspini F, Fumagalli A, et al. The maoxian landslide as seen from space: Detecting precursors of failure with sentinel-1 data. Landslides 2018;15:123-133.

[32] Gan J, Hu J, Li Z, et al. Mapping three-dimensional co-seismic surface deformations associated with the 2015 mw7.2 murghab earthquake based on insar and characteristics of crustal strain. SCIENCE CHINA Earth Sciences 2018;61:1451-1466.

[33] Xu W, Feng G, Meng L, et al. Transpressional rupture cascade of the 2016 mw 7.8 kaikoura earthquake, new zealand. J Geophys Res Solid Earth 2018;123:2396–2409.

[34] Shi X, Wang Y, Jing LZ, et al. How complex is the 2016 mw 7.8 kaikoura earthquake, south island, new zealand? *Sci Bull* 2017;62:309-311.

[35] Fialko Y, Simons M, Agnew D. The complete (3-d) surface displacement field in the epicentral area of the 1999 m w 7.1 hector mine earthquake, california, from space geodetic observations. Geophys Res Lett 2001;28:3063–3066.

[36] Hu J, Li Z, Zhu J, et al. 3d coseismic displacement of 2010 darfield, new zealand earthquake estimated from multi-aperture insar and d-insar measurements. J Geod 2012;86:1029-1041.

[37] Guglielmino F, Nunnari G, Puglisi G, et al. Simultaneous and integrated strain tensor estimation from geodetic and satellite deformation measurements to obtain three-dimensional displacement maps. IEEE Trans Geosci Remote Sens 2011;49:1815-1826.

[38] Hu SW, Xiao BL. Modern theory and application of surveying data processing (in chinese). Beijing, China: Surveying and Mapping Press, 2016

[39] Jiang H, Feng G, Wang T, et al. Toward full exploitation of coherent and incoherent information in sentinel-1 tops data for retrieving surface displacement: Application to the 2016 kumamoto (japan) earthquake. Geophys Res Lett 2017;44:1758–1767.

[40] He P, Wen Y, Xu C, et al. High-quality three-dimensional displacement fields from new-generation sar imagery: Application to the 2017 ezgeleh, iran, earthquake. J Geod 2018;93:573-591.

[41] Cui Y, Ma Z, Aoki Y, et al. Refining slip distribution in moderate earthquakes using sentinel-1 burst overlap interferometry: A case study over may 15, 2020 mw6.5 monte cristo range earthquake (under review). Geophys J

Int 2021.

[42] Li X, Jónsson S, Cao Y. Interseismic deformation from sentinel-1 burst-overlap interferometry: Application to the southern dead sea fault (under review). Geophys Res Lett 2021.

[43] Hooper A. 3-d high-resolution maps of interseismic strain rate from sentinel-1, incorporating along-track measurements. In: Proceedings of the Fringe, 2021.

[44] Xu W. Finite-fault slip model of the 2016 mw 7.5 chiloé earthquake, southern chile, estimated from sentinel-1 data. Geophys Res Lett 2017;44:4774-4780.

[45] Meade BJ. Algorithms for the calculation of exact displacements, strains, and stresses for triangular dislocation elements in a uniform elastic half space. Comput Geosci 2007;33:1064-1075.

[46] Lohman RB, Barnhart WD. Evaluation of earthquake triggering during the 2005–2008 earthquake sequence on qeshm island, iran. J Geophys Res Solid Earth 2010;115.

[47] Khoshmanesh M, Shirzaei M, Nadeau RM. Time-dependent model of aseismic slip on the central san andreas fault from insar time series and repeating earthquakes. J Geophys Res Solid Earth 2015;120:6658-6679.

[48] Lohman RB, Simons M. Some thoughts on the use of insar data to constrain models of surface deformation: Noise structure and data downsampling. Geochem Geophys Geosyst 2005;6.

[49] Murray J, Segall P. Testing time-predictable earthquake recurrence by direct measurement of strain accumulation and release. Nature 2002;419:287-291.

[50] Ji C, Wald DJ. Source description of the 1999 hector mine, california, earthquake, part i: Wavelet domain inversion theory and resolution analysis. Bull Seismol Soc Am 2002;92:1192-1207.

Figure captions

Fig. 1. (a) Colour shaded relief map. The dashed rectangles outline the footprint of SAR data, and the blue rectangle outlines the focused study area (e.g., the range in Fig. 2 and Fig. 4) in this paper. The black lines show the location of known faults, where the east Kunlun active fault belt and the Gande south rim fault zone are labeled. The brown lines are the ruptured fault traces of the 2021 Maduo earthquake, which are manually sketched based on the Sentinel-1 POT observations. The beach ball represents the focal mechanism and epicenter location from the USGS. The location of the Maduo town is represented by the black square. (b) shows the relative position of the Maduo county in Qinghai Province in China.

Fig. 2. Displacements observations along the LOS and AZI directions from ascending/descending, Sentinel-1/ALOS-2 SAR data based on the DInSAR, POT, MAI and BOI methods. Longer and shorter arrows represent the AZI and LOS directions, respectively, and the red arrow corresponds to the observing direction of each observation. The purple lines show the location of ruptured fault traces. The displacements within the range of the whole SAR image are shown in Fig. S1.

Fig. 3. An example of the proposed filtering and interpolating strategy for the ionospheric delay correction with respect to the third beam of the descending ALOS-2 data. (a) The original interferogram. (b) The original RSS-derived ionospheric phase. (c) The original RSS-derived ionospheric phase with the strong fluctuation regions being masked. (d) The ionospheric phase derived by the proposed filtering and interpolating strategy. (e) The interferogram after the ionospheric phase correction. These unwrapped phases are rewrapped here for better display.

Fig. 4. Three-dimensional coseismic displacements of the 2021 Maduo earthquake derived by SM-VCE method.

Circles in (a) and (b) show the locations of the GNSS stations, and their color indicates the GNSS-observed displacement. The arrows in (c) are the down-sampled horizontal displacements. The 3-D displacements within a greater range are shown in Fig. S4.

Fig. 5. Three strain invariants for the 2021 Maduo earthquake. In (a), the crosses represent the maximum and minimum normal strains, where the arrow orientation and the arrow length are the direction and magnitude of the strains, respectively. The extensional and compressional strains are shown as the inward and outward arrows, respectively. In (b), the rotational wedges are presented to better illuminate the magnitude and direction of the rotation. In (c), the direction of the double-sided arrow represents the direction of the maximum shear. The strain fields within a greater range are shown in Fig. S6.

Fig. 6. Slip distribution derived from the constraints of our derived 3-D displacements. (a) is the front view of the slip distribution of two faults. (b) is the back view for a better view on the long fault. Red stars represent the location of hypocenter.

Tables

Table 1. Basic information of the SAR data used herein

Sensor	Orbit direction	Master-slave date	Spatial perpendicular baseline (m)	Wavelength (cm)	Incident angle (deg.)	Azimuth angle (deg.)	Imaging mode
Sentinel-1	As	20210520-20210526	54	5.6	39.5	-13.0	TOPS
Sentinel-1	Des	20210520-20210526	109	5.6	39.6	-167.0	TOPS
ALOS-2	As	20200525-20210524	-190	23.6	36.2	-12.7	Strip-map
ALOS-2	Des	20201204-20210604	197	23.6	39.0	-170.0	ScanSAR